Lattice Boltzmann Simulations of Multiple Droplet Interactions During Impingement on the Substrate

Wenchao Zhou[1], Drew Loney[1], Andrei G. Fedorov[1,2], F. Levent Degertekin[1,2], David W. Rosen[1]

[1]The George W. Woodruff School of Mechanical Engineering

[2]Parker H. Petit Institute for Bioengineering and Bioscience

Georgia Institute of Technology, 813 Ferst Drive, Atlanta, GA, 30332-0405, USA

Abstract

Studying material interface evolution in the course of multiple droplet interactions is critical for understanding the material additive process in inkjet deposition. In this paper, we have developed a novel numerical model based on the Lattice Boltzmann Method (LBM) to simulate the interface dynamics during impingement and interaction of multiple droplets. A lattice Boltzmann formulation is proposed to solve the governing equations of the continuous phase-field model that are used in commercial software COMSOL. The LBM inter-particle force is derived by comparing the recovered macroscopic equations from LBM equations with the governing equations of the phase-field model. In addition, a new set of boundary conditions for the LBM formulation is proposed based on conservation of mass and momentum to ensure correct evolution of contact line dynamics. The results of LBM simulations are compared with those of COMSOL and experimental data from literature. The comparison shows the proposed LBM model not only yields a significant improvement in computational speed, but also results in better accuracy than COMSOL as validated against the experiments. We have also demonstrated the capability of the developed LBM numerical solver for simulating interactions between multiple droplets impinging on the substrate, which is critical for development and optimization of inkjet manufacturing.

1 INTRODUCTION

Inkjet deposition is an emerging technology that enables more economic and scalable manufacturing than other additive techniques. Studying the interface dynamics of multiple droplet interaction is crucial to understanding droplet deposition process and control of manufacturing results. Droplet impingement has been extensively studied for over a century [1]. Numerous research advances have been reported, including experimental observations [2-5], analytical modeling [6-9], and numerical simulations [10-14].

However, most of previous research focused on single droplet impingement, which is only marginally relevant to manufacturing. The computational cost for simulating droplet impingement in three-dimensional settings prohibits the study of multiple-droplet impingement, which can potentially cast more insights into the manufacturing process of inkjet deposition. An enabling numerical tool for simulating multiple-droplet impingement is critical for advancing inkjet deposition technology. Lattice Boltzmann Method (LBM) is a promising alternative to conventional computational fluid dynamics (CFD) simulations for its computational efficiency and has experienced rapid development during the past two decades. Originating from Lattice-Gas Automata for simulating gas dynamics [15], the LBM is a particle-based method that treats

a group of molecules as a fluid particle rather than continuum and solves the dynamics of particle populations that comes from a microscopic description of the fluid behavior. The LBM has been widely used to model multiphase flow and interface phenomena. A number of approaches for modeling inter-particle interaction have been proposed, of which the three models have achieved significant success - the "Shan-Chen" (SC) model [16-17] that mimics the intermolecular interactions with an empirical forcing "potential" function to correct the velocity field after each time step, the "free-energy-based" model [18-19] that incorporates the thermodynamic effects of complex fluids into a modified equilibrium distribution function resulting from a modified momentum flux tensor using the concepts of free-energy functional, and the "He-Shan-Doolen" (HSD) model [20-21] that provides a solid theoretical foundation for a transition from the continuous Boltzmann equation to the lattice Boltzmann equation and a different perspective of viewing LBM as a special finite difference approximation of the Boltzmann equation. The well-known numerical instability problem arising from the spurious flow around the interface of multiphase flow, especially in the case of high density and/or viscosity mismatch, has been tackled by different research groups [22-24]. Briant et al. proposed a free energy-based wetting boundary conditions to simulate the contact line dynamics [25-26]. Inamuro et al. and Yan et al. studied spontaneous water drop spreading on both homogeneous and heterogeneous partially wetting surfaces [22, 24]. Although the equlibrium profiles of the spreading droplets matched well with prediction, the transient profiles were not compared with either experiments or other theoretical treatments. Lee and Liu [27] reported transient LBM simulation of high-speed droplet impingement with Weber number and Reynolds number over 100 and 650 respectively and used a slightly different definition of the spreading factor from the experiments in order to match the experimental data. In most of previous studies concerning a droplet on a solid wall, a surface energy formulation was used for partial-wetting boundary condition, which may cause a discrepancy between the prescribed contact angle and the computed contact angle [28]. In addition, either the popular "bounced-back" scheme [24-25, 29] or an "equilibrium bounced-back" scheme [27] were used for the velocity boundary condition at the wall, which did not conserve momentum at the boundary [30]. In this paper, we propose a LBM formulation based on the HSD model with a new set of boundary conditions, which are rigorously derived based on first principles and consistent with the boundary conditions used in classical continuous formulation to ensure conservation of both mass and momentum at the wall boundary. The proposed LBM formulation can recover the governing equations of the phase-field model used in commercial software COMSOL [31] by Chapman-Enskog multiscale analysis [32] and therefore provide an alternative to solve the equations, which prove to be significantly faster and more accurate than COMSOL. The simulation results for 3D droplet impingement dynamics and interface evolution upon interactions with substrate were compared with that those predicted by COMSOL and with experimental data from literature [33]. Finally, the cases of multiple interacting droplets in 3D, including two-droplet, a-line-of-droplet, and an-array-of-droplet impingements have been successfully simulated and used to demonstrate the new capabilities enabled by the proposed LBM simulation algorithm. The capability for simulating impingment of a line of droplets can be used to optimize printing conductive lines to improve printed electronics, for example. Simulating an-array-of-droplet impingement can be important to thin-film patterning for a number of important industrial applications, such as thin-film transistor printing, surface coating, and a layer for additive manufacturing.

The rest of the paper is organized as follows. In section 2, the proposed LBM formulation is presented. Section 3 presents an approach for self-consistent implementation of the boundary conditions. In section 4, the LBM simulation results are compared with predictions of COMSOL

simulations and validated against the experimental data. Section 5 demonstrates the capability of the proposed LBM numerical model to simulate the multiple droplet impingement and interactions in 3D. Conclusions are given in section 6.

2 LATTICE BOLTZMANN FORMULATION

2.1 *Review*

The LBM solves macroscopic motion of a fluid by following the evolution of a lattice Boltzmann equation that governs the behavior of the single-particle distribution function [21],

$$\frac{\partial f_i}{\partial t} + \mathbf{e}_i \cdot \nabla f_i = -\frac{f_i - f_i^{(0)}}{\lambda} + \mathbf{F} \cdot \frac{\mathbf{e}_i - \mathbf{u}}{\rho c_s^2} f_i^{(0)} \tag{1}$$

where $f_i \equiv f_i(\mathbf{x}, \mathbf{e}_i, t)$ is the single-particle distribution function, $\mathbf{x}$ is the spatial coordinates, $\mathbf{e}_i$ is the local particle velocity in the ith direction of a discretized velocity space, λ is the time scale for local particle distribution relaxing back to its equilibrium state, $\mathbf{F}$ is the external body force exerted on a particle, ρ is fluid density, c_s is the lattice speed of sound, which is a scaling factor that depends on the specific lattice structure [34], $\mathbf{u}$ is the macroscopic velocity of fluid, and $f_i^{(0)}$ is the equilibrium distribution function. The equilibrium distribution is approximated by expanding the Maxwellian distribution to the second order of macroscopic velocity $\mathbf{u}$:

$$f_i^{(0)} = t_i \rho \left[1 + \frac{\mathbf{e}_i \cdot \mathbf{u}}{c_s^2} + \frac{(\mathbf{e}_i \cdot \mathbf{u})^2}{2c_s^4} - \frac{\mathbf{u} \cdot \mathbf{u}}{2c_s^2} \right] \tag{2}$$

where t_i is the weighting factor that depends on the specific lattice model, which is usually identified as *d*-dimensional *b*-velocity *DdQb* model. A summary of different lattice models can be found in [35]. The lattice symmetry produces the following relationships:

$$\sum t_i = 1; \ \sum t_i \mathbf{e}_i = 0; \ \sum t_i \mathbf{e}_i \mathbf{e}_i = c_s^2 \delta_{\alpha\beta}; \ \sum t_i \mathbf{e}_i \mathbf{e}_i \mathbf{e}_i = 0;$$

$$\sum t_i \mathbf{e}_i \mathbf{e}_i \mathbf{e}_i \mathbf{e}_i = c_s^4 [\delta_{\alpha\beta} \delta_{\gamma\delta} + \delta_{\alpha\gamma} \delta_{\beta\delta} + \delta_{\alpha\delta} \delta_{\beta\gamma}]; \ \sum t_i \mathbf{e}_i \mathbf{e}_i \mathbf{e}_i \mathbf{e}_i \mathbf{e}_i = 0 \tag{3}$$

where $\delta_{\alpha\beta}$ is the Kronecker delta. The hydrodynamic variables on each node are defined as moments of distribution function:

$$\rho = \sum f_i \ ; \ \rho\mathbf{u} = \sum f_i \mathbf{e}_i \ ; \ \mathbf{\Pi} = \sum f_i \mathbf{e}_i \mathbf{e}_i \tag{4}$$

where $\rho\mathbf{u}$ is the fluid momentum vector, and tensor $\mathbf{\Pi}$ is identified as momentum flux.

2.2 *Discrete Boltzmann Equations*

Now only $\mathbf{F}$ in Eq. (1) is left undetermined. He et al. [20] derived a formula for $\mathbf{F}$ by considering the intermolecular attraction and exclusion-volume effect from a microscopic perspective. Alternatively, we will derive $\mathbf{F}$ by comparing the macroscopic transport equations recovered from Eq. (1) with the governing equations of the phase-field model used in conventional continuous formulation [31] in order to ensure self-consistency of the LBM approach. Similar to traditional CFD algorithms (e.g., a SIMPLE algorithm [36]) that do not

update pressure field using the equation of state (EOS), a new distribution function is first introduced by He et al. [20] to directly track pressure evolution:

$$g_i = f_i c_s^2 + \psi(\rho)\Gamma_i(0); \quad g_i^{(0)} = f_i^{(0)}c_s^2 + \psi(\rho)\Gamma_i(0) \tag{5}$$

where

$$\Gamma_i(\mathbf{u}) = \frac{f_i^{(0)}}{\rho}; \quad \psi(\rho) = p - \rho c_s^2 \tag{6}$$

where p is the thermodynamic pressure for non-ideal fluids, which is only function of density ρ under isothermal condition. It should be noted that when fluid is in motion (that is, not in thermodynamic equilibrium), a hydrodynamic pressure will develop, which is on the order of $\rho \mathbf{u}^2$ based on Bernoulli's principle. Since thermodynamic pressure is on the order of ρc_s^2, the hydrodynamic pressure is neglected under incompressible limit (i.e., $\mathbf{u} \ll c_s$). Combining Eqs. (1), (3), (4), and (5), and using algebraic manipulations, yields:

$$\frac{\partial g_i}{\partial t} + \mathbf{e}_i \cdot \nabla g_i = -\frac{g_i - g_i^{(0)}}{\lambda} + (\mathbf{e}_i - \mathbf{u}) \cdot [\Gamma_i(\mathbf{u}) \cdot \mathbf{F} + \Gamma_i(0) \cdot \nabla\psi(\rho)] \tag{7}$$

$$p = \sum g_i; \quad \rho\mathbf{u}c_s^2 = \sum g_i \mathbf{e}_i \tag{8}$$

$$\sum g_i^{(0)} = p; \quad \sum g_i^{(0)} \mathbf{e}_i = \rho\mathbf{u}c_s^2 \tag{9}$$

Next we apply the Chapman-Enskog multiscale analysis to Eq. (7) by expanding:

$$g_i = g_i^{(0)} + \epsilon g_i^{(1)} + \epsilon^2 g_i^{(2)} + O(\epsilon^3) \tag{10}$$

where ϵ is identified as the Knudsen number, which is introduced in the Chapman-Enskog theory to keep track of the order of the terms in the series. Higher order terms represent the influence from a longer time scale and larger spatial scale. Then we can recover the macroscopic equations:

$$\frac{\partial p}{\partial t} + \mathbf{u} \cdot \nabla p + \rho c_s^2 \nabla \cdot \mathbf{u} = 0 \tag{11}$$

$$\frac{\partial}{\partial t}(\rho\mathbf{u}) + \frac{1}{c_s^2}\nabla \cdot (\mathbf{\Pi}_g^{(0)} + \mathbf{\Pi}_g^{(1)}) = \mathbf{F} + \nabla\psi(\rho) \tag{12}$$

where

$$\mathbf{\Pi}_g = \sum g_i \mathbf{e}_i \mathbf{e}_i \tag{13}$$

$$\mathbf{\Pi}_g^{(0)} = \sum g_i^{(0)} \mathbf{e}_i \mathbf{e}_i = c_s^2 p\mathbf{I} + \rho c_s^2 \mathbf{u}\mathbf{u} \tag{14}$$

$$\mathbf{\Pi}_g^{(1)} = \sum g_i^{(1)} \mathbf{e}_i \mathbf{e}_i = -\lambda c_s^4 (\nabla\rho\mathbf{u} + (\nabla\rho\mathbf{u})^T) \tag{15}$$

where $\mathbf{I}$ is the identity matrix, and

$$g_i^{(1)} = -t_i\lambda\left[\mathbf{Q}_i : \nabla\rho\mathbf{u} + \mathbf{e}_i \cdot \nabla\psi(\rho) - \mathbf{e}_i\nabla: \rho\mathbf{uu} + \frac{1}{2c_s^2}\left((\mathbf{e}_i \cdot \nabla)(\mathbf{Q}_i : \rho\mathbf{uu})\right)\right] \tag{16}$$

where $\mathbf{Q}_i = \mathbf{e}_i\mathbf{e}_i - c_s^2\mathbf{I}$. Since p is a function of ρ for isothermal fluid, the material derivative of p is negligible under incompressibility limit, and Eq. (11) is thus equivalent to the mass conservation equation for incompressible fluids at constant temperature. Plugging Eqs. (14) and (15) back into Eq. (12) leads to:

$$\frac{\partial}{\partial t}(\rho\mathbf{u}) + \nabla \cdot (\rho\mathbf{uu}) = -\nabla p + \nabla \cdot \left(\lambda c_s^2(\nabla\rho\mathbf{u} + (\nabla\rho\mathbf{u})^T)\right) + \mathbf{F} + \nabla\psi(\rho) \tag{17}$$

It is interesting to point out that $\mathbf{\Pi}_g^{(1)}$ is recovered from the $O(\epsilon^1)$ order component of g_i and is dependent on velocity gradients, which is consistent with the microscopic view of $g_i^{(1)}$. Comparing with the momentum equation of the phase-field model used in COMSOL, we can then derive:

$$\nu = \lambda c_s^2 \tag{18}$$

$$\mathbf{F} = -\nabla\psi(\rho) + \mu\nabla C + \rho\mathbf{g} \tag{19}$$

where ν is the kinematic viscosity, C is the phase composition of the fluid, $\mathbf{g}$ is the gravity, and μ is the chemical potential defined as derivative of Gibbs free energy with respect to C at constant temperature and pressure. The free energy takes the Ginzburg-Landau form for two-phase flow [37]:

$$E(C, \nabla C) = \beta(C - C_l)^2(C - C_h)^2 + \frac{\kappa}{2}|\nabla C|^2 \tag{20}$$

where the first term on the right hand side is the bulk free energy E_0 that acts to separate the phases, the second term is the gradient energy that favors mixing the phases together, β is a constant relating to bulk free energy, C_l and C_h are two constants representing two different phases (here we choose $C_l = 0$ for surrounding air and $C_h = 1$ for liquid), and κ is a parameter related to surface tension σ. Minimizing the free energy of the system leads to a constant chemical potential from calculus of variation:

$$\mu = 4\beta(C - C_l)(C - C_m)(C - C_h) + \kappa\nabla^2 C \tag{21}$$

where $C_m = (C_l + C_h)/2$. For a plane interface under equilibrium, we can obtain a composition profile across interface from Eq. (21):

$$C(z) = \frac{C_h + C_l}{2} + \frac{C_h - C_l}{2}\tanh\left(\frac{2z}{\xi}\right) \tag{22}$$

where z is the coordinate normal to the interface, and ξ is the interface thickness, which is given by:

$$\xi = \frac{4}{C_h - C_l}\sqrt{\frac{\kappa}{2\beta}} \tag{23}$$

With the composition profile given by Eq. (38), we can obtain the surface tension by integrating the free energy across the interface:

$$\sigma = \frac{(C_h - C_l)^3}{6}\sqrt{2\kappa\beta} \tag{24}$$

Because there is large variation in C, but a little difference in μ across the interface under equilibrium, we replace the surface tension term $\mu\nabla C$ in **F** (Eq. (19)) with $-C\nabla\mu$ using the identity $\mu\nabla C = -C\nabla\mu$ [38] to reduce numerical errors around the interface.

Next a second distribution function is introduced [27] to track the evolution of C:

$$h_i = \frac{C}{\rho}f_i; \ h_i^{(0)} = \frac{C}{\rho}f_i^{(0)} \tag{25}$$

The partial differential equation governing the evolution of composition C is the Cahn-Hilliard diffusion convection equation:

$$\frac{\partial C}{\partial t} + \mathbf{u}\cdot\nabla C = \nabla\cdot M\nabla\mu \tag{26}$$

where M is mobility. We can derive the evolution equation for h_i with Eqs. (1), (25), and (26),

$$\frac{\partial h_i}{\partial t} + \mathbf{e}_i\cdot\nabla h_i = -\frac{h_i - h_i^{(0)}}{\lambda} + (\mathbf{e}_i - \mathbf{u})\cdot\left(\frac{C}{\rho c_s^2}\mathbf{F} + \nabla C - \frac{C}{\rho}\nabla\rho\right)\Gamma_i(\mathbf{u}) + \Gamma_i(\mathbf{u})\nabla\cdot M\nabla\mu \tag{27}$$

$$\sum h_i = C; \ \sum h_i\mathbf{e}_i = C\mathbf{u} \tag{28}$$

$$\sum h_i^{(0)} = C; \ \sum h_i^{(0)}\mathbf{e}_i = C\mathbf{u} \tag{29}$$

In the same way we can apply the Chapman-Enskog multiscale analysis to Eq. (27), which leads to Eq. (26). Two points should be noted: first, the diffusion process driven by the chemical potential difference is assumed to occur on a longer time scale than the particle collision; second, to recover the Cahn-Hilliard equation only the 0th and 1st order velocity moments of the distribution function h_i (Eq. (28)) are used to link the microscopic description of the particle motion to the macroscopic fluid motion, while to recover the mass and momentum conservation equations (Eqs. (11) and (17)) the 0th, 1st, and 2nd order velocity moments of the distribution function g_i (Eqs. (8), and (13)) are used, which has important implications for boundary conditions. That is, the boundary conditions for the distribution functions need to maintain the same relationships between the distribution functions and the macroscopic quantities in the velocity moments.

2.3 Lattice Boltzmann Equations

To solve the evolution equations for g_i (Eq. (7)) and h_i (Eq. (27)), we can apply the trapezoidal rule to integrate over each time step δt along the characteristic direction given by $\mathbf{e_i}$:

$$g_i(\boldsymbol{x} + \mathbf{e_i}\delta t, t + \delta t) - g_i(\boldsymbol{x}, t) \tag{30}$$

$$= -\frac{1}{2\tau}[(g_i - g_i^{(0)})|_{\boldsymbol{x}+\mathbf{e_i}\delta t, t+\delta t} - (g_i - g_i^{(0)})|_{\boldsymbol{x},t}]$$

$$+ \frac{\delta t}{2}[gt_i|_{\boldsymbol{x}+\mathbf{e_i}\delta t, t+\delta t} + gt_i|_{\boldsymbol{x},t}]$$

$$h_i(\boldsymbol{x} + \mathbf{e_i}\delta t, t + \delta t) - h_i(\boldsymbol{x}, t) \tag{31}$$

$$= -\frac{1}{2\tau}[(h_i - h_i^{(0)})|_{\boldsymbol{x}+\mathbf{e_i}\delta t, t+\delta t} - (h_i - h_i^{(0)})|_{\boldsymbol{x},t}] + \frac{\delta t}{2}[ht_i|_{\boldsymbol{x}+\mathbf{e_i}\delta t, t+\delta t}$$

$$+ ht_i|_{\boldsymbol{x},t}]$$

where $\tau = \lambda/\delta t$ is the dimensionless relaxation time,

$$gt_i = (\mathbf{e_i} - \mathbf{u}) \cdot [\Gamma_i(\mathbf{u}) \cdot \mathbf{F} + \Gamma_i(0) \cdot \nabla\psi(\rho)], \tag{32}$$

$$ht_i = (\mathbf{e_i} - \mathbf{u}) \cdot \left(\frac{C}{\rho c_s^2}\mathbf{F} + \nabla C - \frac{C}{\rho}\nabla\rho\right)\Gamma_i(\mathbf{u}) + \Gamma_i(\mathbf{u})\nabla \cdot M\nabla\mu \tag{33}$$

To maintain an explicit scheme, the modified distribution functions are introduced:

$$\bar{g}_i = g_i + \frac{1}{2\tau}\left(g_i - g_i^{(0)}\right) - \frac{\delta t}{2}gt_i \tag{34}$$

$$\bar{g}_i^{(0)} = g_i^{(0)} - \frac{\delta t}{2}gt_i \tag{35}$$

$$\bar{h}_i = h_i + \frac{1}{2\tau}\left(h_i - h_i^{(0)}\right) - \frac{\delta t}{2}ht_i \tag{36}$$

$$\bar{h}_i^{(0)} = h_i^{(0)} - \frac{\delta t}{2}ht_i \tag{37}$$

Then the evolution equations (30) and (31) become:

$$\bar{g}_i(\boldsymbol{x} + \mathbf{e_i}\delta t, t + \delta t) - \bar{g}_i(\boldsymbol{x}, t) = -\frac{1}{\tau + 0.5}\left(\bar{g}_i - \bar{g}_i^{(0)}\right)|_{\boldsymbol{x},t} + \delta t gt_i|_{\boldsymbol{x},t} \tag{38}$$

$$\bar{h}_i(\boldsymbol{x} + \mathbf{e_i}\delta t, t + \delta t) - \bar{h}_i(\boldsymbol{x}, t) = -\frac{1}{\tau + 0.5}\left(\bar{h}_i - \bar{h}_i^{(0)}\right)|_{\boldsymbol{x},t} + \delta t ht_i|_{\boldsymbol{x},t} \tag{39}$$

With Eqs. (8), (28), (34), and (36), we can obtain:

$$C = \sum \bar{h}_i + \frac{\delta t}{2}\nabla \cdot M\nabla\mu \tag{40}$$

$$p = \sum \bar{g}_i - \frac{\delta t}{2}\mathbf{u} \cdot \nabla\psi(\rho) \tag{41}$$

$$\rho\mathbf{u} = \frac{1}{c_s^2}\sum \bar{g}_i\mathbf{e_i} - \frac{\delta t}{2}C\nabla\mu \tag{42}$$

Note that in Eqs. (40) and (41) we use μ and p from previous time step to avoid implicitness, which still gives a second order accuracy in time [39]. The density and relaxation time across the interface can be calculated as:

$$\rho = \frac{C - C_l}{C_h - C_l}(\rho_h - \rho_l) + \rho_l \tag{43}$$

$$\tau = \frac{\left(\frac{C - C_l}{C_h - C_l}\right)^2 (\rho_h \tau_h - \rho_l \tau_l) + \rho_l \tau_l}{\left(\frac{C - C_l}{C_h - C_l}\right)^2 (\rho_h - \rho_l) + \rho_l} \tag{44}$$

where the subscripts h and l stand for the two different phases.

3 BOUNDARY CONDITIONS

To simulate droplets impinging onto a solid wall, we need to implement the two wall boundary conditions, including partial wetting boundary conditions for the equilibrium contact angle and the velocity boundary conditions at the wall.

3.1 *Partial Wetting Boundary Conditions*

For most previous studies, a surface energy formulation for computation of the contact angle is employed by taking into account the wall free energy through linear, quadratic, or cubic approximations [25, 27]. A geometric formulation for the wetting condition is mathematically equivalent to the surface energy formulation, but computationally more efficient and more accurate in numerical discretization because the surface energy formulation usually causes a discrepancy between the prescribed contact angle and the computed contact angle [28]. Although the geometric formulation has not been adopted in the LBM community yet, a number of traditional CFD algorithms based on continuous form of governing transport equations have successfully adopted it, including implementation by COMSOL. To be consistent with COMSOL implementation of the contact angle treatment, which will be used for validation of the LBM algorithm proposed here, we also adopt the geometric formulation of the wetting boundary condition. The geometric relationships are illustrated in Figure 1:
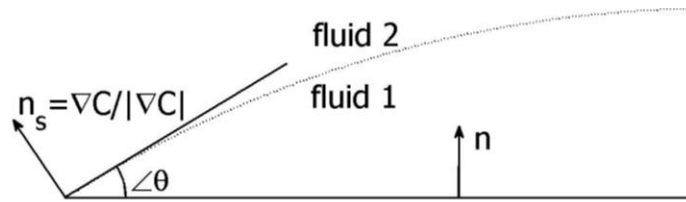

Figure 1. Illustration of the geometric relationships of a contact angle

$$\mathbf{n}_s = \frac{\nabla C}{|\nabla C|} \tag{45}$$

where $\mathbf{n}_s$ is the outer normal to the interface.

$$\tan\left(\frac{\pi}{2} - \theta\right) = \frac{\mathbf{n}_s \cdot \mathbf{n}}{|\mathbf{n}_s - (\mathbf{n}_s \cdot \mathbf{n})\mathbf{n}|} = \frac{\mathbf{n} \cdot \nabla C}{|\nabla C - (\mathbf{n} \cdot \nabla C)\mathbf{n}|} \tag{46}$$

where θ is the equilibrium contact angle, and **n** is the normal to the wall. A second boundary condition is required to ensure there is no mass flux across the non-permeable wall:

$$\mathbf{n} \cdot \nabla \mu|_{\text{wall}} = 0 \qquad (47)$$

3.2 *Velocity Boundary Conditions*

It is straightforward to apply a Dirichlet velocity boundary condition for incompressible Navier-Stokes equations because Navier-Stokes equations explicitly solve for the velocity field. On the other hand, LBM solves the evolution of particle populations that have more degrees of freedom than what can be imposed by the constraints of the velocity boundary condition. Therefore, it can be complicated to translate the velocity boundary conditions in the continuous formulation into the equivalent boundary conditions for the particle populations. Many previous studies chose the popular bounce-back scheme for the non-slip wall boundary conditions due to its simplicity [24-25], but it has a fundamental deficiency of not conserving momentum at the boundary [30]. To resolve this deficiency in LBM computations, the boundary conditions are implemented by finding the appropriate particle population distribution at each computational node near the wall after the streaming step, as illustrated by the dashed vectors in Figure 2, such that the constraints imposed by the specified velocity at the boundary are enforced.
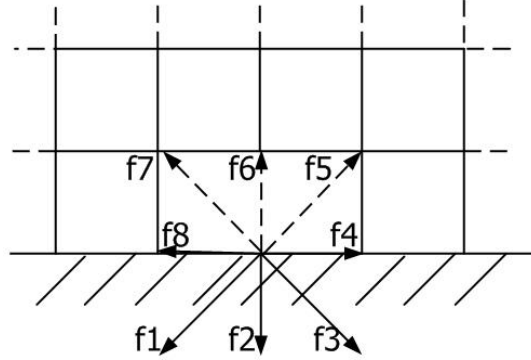

Figure 2. Illustration of particle populations on the wall boundary. The dashed vectors stand for incoming unknown particle populations after streaming step.

It should be noted that the proposed LBM formulation solves for evolution of the modified distribution functions $\bar{g}_i$ and $\bar{h}_i$, which are used for convenience of calculations and do not have clear physical meanings. However, all the constraints from boundary conditions only apply to the original distribution functions g_i and h_i. Therefore, to implement the boundary conditions in our LBM simulations, we need to first obtain g_i and h_i from $\bar{g}_i$ and $\bar{h}_i$, apply all constraints to find out the unknown g_i and h_i, and then calculate the unknown $\bar{g}_i$ and $\bar{h}_i$ with Eqs. (34), (35), (36), and (37). We will explain how to determine the unknown g_i and h_i in the following.

After the streaming step, we know the prescribed velocity **u** at the boundary, the outgoing particle populations g_+ and h_+, the particle populations parallel to the wall g_0 and h_0, the constraints between the particle populations and macroscopic quantities that are required to recover macroscopic equations as in Eqs. (8), (13), and (28). So, the unknown incoming particle populations g_- and h_- are the quantities that need to be solved for to satisfy the boundary conditions.

First, we can find out the macroscopic quantity C with known particle populations and Eq. (28):

$$C = \sum h_i = h_+ + h_0 + h_- \tag{48}$$

$$C\mathbf{u}_n = \sum h_i \mathbf{e}_i = h_+ - h_- \tag{49}$$

where $\mathbf{u}_n$ is the velocity normal to the wall. Therefore we can obtain:

$$C = \frac{1}{1 + \mathbf{u}_n}\,(2h_+ + h_0) \tag{50}$$

Then the density ρ on the boundary can be obtained from Eq. (43) and pressure p can be found from Eq. (8). With the macroscopic quantities C, ρ, p, and $\mathbf{u}$ known on the boundary, one needs to find a set of particle populations g_i and h_i that satisfy Eqs. (8), (13), and (28). A tempting approach is to replace all the particle populations on the boundary with their equilibrium distributions $g_i^{(0)}$ and $h_i^{(0)}$. According to Eqs. (9), and (29), this approach will satisfy Eqs. (8), and (28), but it will change Eq. (13) to Eq. (14). The $\mathbf{\Pi}_g^{(1)}$ component that attributes to the momentum flux due to the viscosity effects will be missing from the recovered equations and thus the momentum will not be conserved at the boundary. Therefore, we need to include the contribution of the $O(\epsilon^1)$ component of g_i that can be reconstructed at the boundary as:

$$g_i = g_i^{(0)}(p, \rho, \mathbf{u}) + g_i^{(1)} \tag{51}$$

where $g_i^{(1)}$ can be obtained from Eq. (31) which can be approximated by:

$$g_i^{(1)} = -t_i \rho \lambda (\mathbf{Q}_i : \nabla \mathbf{u}) \tag{52}$$

and leads to the same recovered tensor $\mathbf{\Pi}_g^{(1)}$.

4 RESULTS AND VALIDATION

We have implemented a 3D numerical solver based on our proposed LBM scheme with a D3Q19 lattice model to simulate droplet impingement on a solid surface, which has shown a significant speed improvement over traditional CFD algorithms based on the continuous phase-field model, as implemented for example by the commercial software COMSOL. We have tested three different cases with different contact angles for a single droplet impingement to compare with COMSOL simulation results and experimental data in [33]. The droplet size is 48.8μm and the impact speed is 4.36m/s. The fluid properties of the liquid droplet and the surrounding gas are taken as the properties of water and air at 1 atm and 25 °C. The Weber number is 12.8 and the Ohnesorge number is 0.0151. The contact angles for the three cases are 31 °, 90 °, and 107 ° respectively. For all the LBM simulations, the computational domain is set to be 100×100×70 and the droplet radius is set to be 25 LB units. Although the LBM has the advantage for massive parallelization due to the locality of the computations, all reported simulations are run on a single thread on a laptop PC with a memory requirement slightly over 1GB for each simulation and are completed within 20 hours for each case. For a similar mesh density (i.e., spatial resolution of computations), it would roughly take over 1 month for COMSOL to run the same 3D simulation on a 16-core cluster with over 100GB memory requirement based on our experience. Therefore, all the COMSOL simulations presented here were performed with a 2D axi-symmetrical model [14, 40].

The comparison of the dimensionless spreading factor D*, droplet height H*, and the shape coefficient, as predicted by our LBM and COMSOL simulations, as well as the LBM simulations by Lee et al. reported in literature [27], against the experimental data are presented in Figure 3 through Figure 5. The spreading factor is defined as the ratio of the diameter of the wetted area to the droplet diameter, the dimensionless droplet height is defined as the ratio of the height of the droplet above the substrate to the droplet diameter, and the shape coefficient is a novel metric that we developed to quantify the droplet shape [14, 41]. Note that in Lee et al.'s results [27], the spreading factor is defined as the ratio of the spreading diameter to the droplet diameter where the spreading diameter is the blob diameter when the droplet spreads and the diameter of the wetted area when droplet retracts, which is different from the definition of the spreading factor in the experiments. We can see that overall the results agree very well in all three cases. There is an excellent agreement in time evolution of the spreading factor between our LBM simulations and COMSOL simulations, while the COMSOL simulations and the literature LBM simulations fail to capture the details of the droplet height change, which is particularly evident in Cases 2 and 3 as shown in Figure 4 and Figure 5 respectively, for the later times after 10μs to 20μs, which leads to a discrepancy in the shape coefficient as well as shown on the right hand side of Figure 3 through Figure 5. But overall the evolutions of the shape coefficient that characterizes the overall droplet shape, match well between our LBM simulations and COMSOL, which establishes the consistency of our LBM formulation with the phase-field model in COMSOL. We can also see that for Cases 1 and 2, as shown in Figure 3 and Figure 4, respectively, both the LBM and COMSOL simulations fail to capture the oscillations of the droplet height. One possible reason is that the contact line pinning due to possible surface contamination could cause the discrepancy of the final equilibrium spreading factor during experiments and affect the overall interface dynamics that is responsible for the droplet height oscillation.
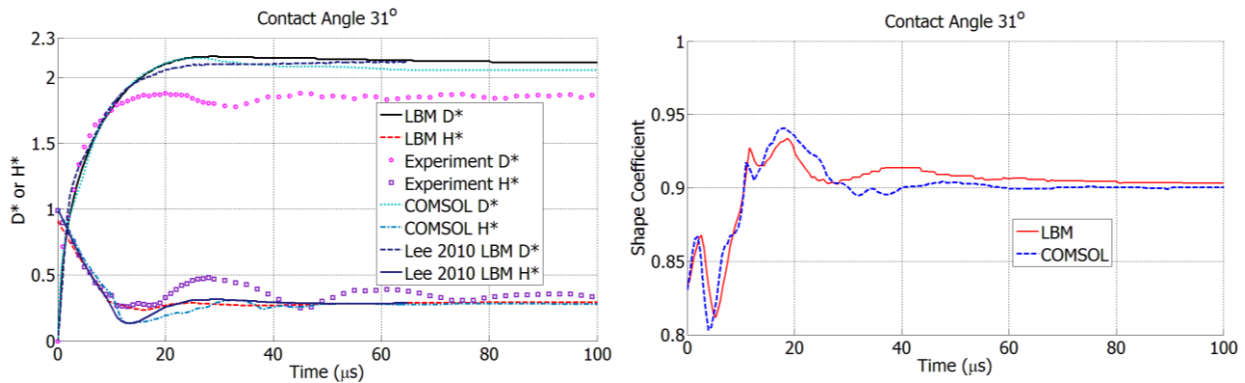

Figure 3. Left: Validation of spreading factor D* and dimensionless droplet height H* for Case 1; Right: Comparison of shape coefficient change between LBM and COMSOL simulations for Case 1
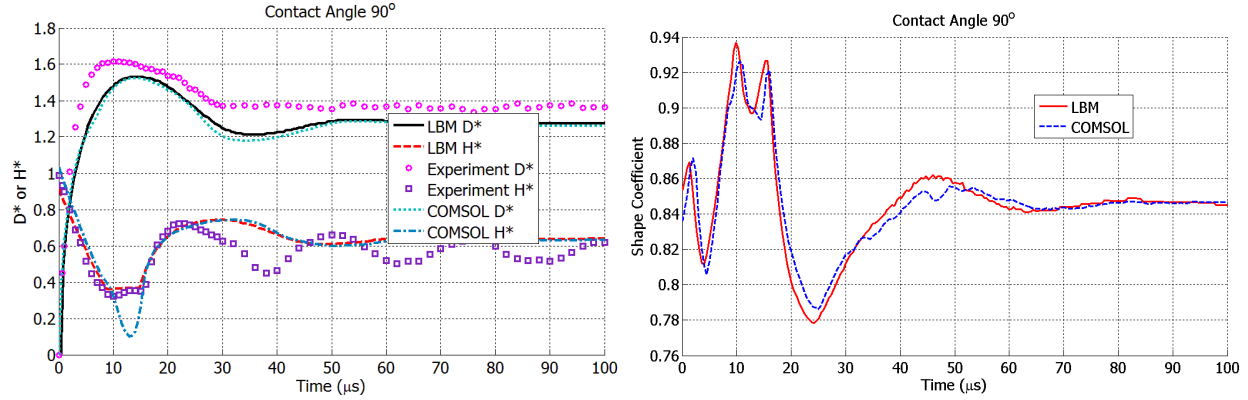
Figure 4. Left: Validation of spreading factor D* and dimensionless droplet height H* for Case 2; Right: Comparison of shape coefficient change between LBM and COMSOL simulations for Case 2

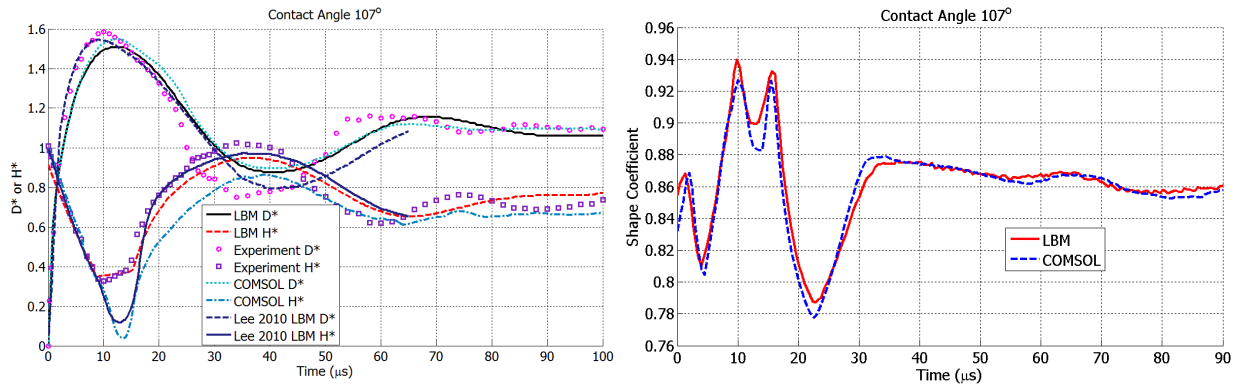Figure 5. Left: Validation of spreading factor D* and dimensionless droplet height H* for Case 3; Right: Comparison of shape coefficient change between LBM and COMSOL simulations for Case 3

5 MULTIPLE DROPLET IMPINGEMENT

The validity and computational efficiency of our numerical solver for simulating 3D droplet impingement open up the possibility for studying multiple-droplet impingement. We exemplify this capability with three different simulation cases, including an impingement of two interacting droplets as shown in Figure 6, a-line-of-multiple-droplet impingement as shown in Figure 7, and a-square-array-of-droplet impingement as shown in Figure 8. The droplet diameter is set to be 50 μm, the impact velocity is 10m/s, and the contact angle is 90° for all cases. The distance between the centroids of the droplets for cases 1 and 3 is set to 80 μm, and it is equal to 65 μm for case 2. The Weber number is 100 and Ohnesorge number is 0.04, so the simulations are focusing on inertia dominated hydrodynamics, with more important effect of surface tension on the droplet shape evolution as compared to viscous forces. As it can be seen from evolution of droplet shapes presented in Figures 17-19, including coalescence events, the interface topology and dynamics are highly complex, especially with an increase in the number of interacting droplets. Importantly, not only our numerical LBM solver effectively captures the numerical complexity of the physical problem, but also preserves some inherent symmetries of each simulation case even though the simulations were performed in general 3D format. It is interesting to see that the interfacial patterns for the first two cases follow an a priori expected behavior, but shows some unusual intermediate states for the third case.
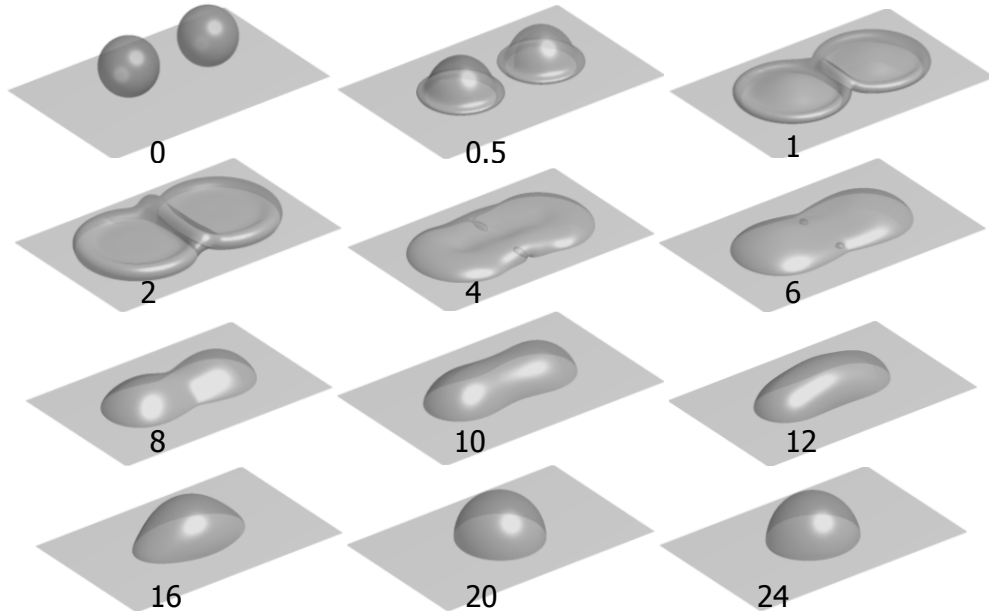
Figure 6. Demonstration of two-droplet impingement in the unit of dimensionless time (We = 100; Oh = 0.04; droplet distance = 80 μm).
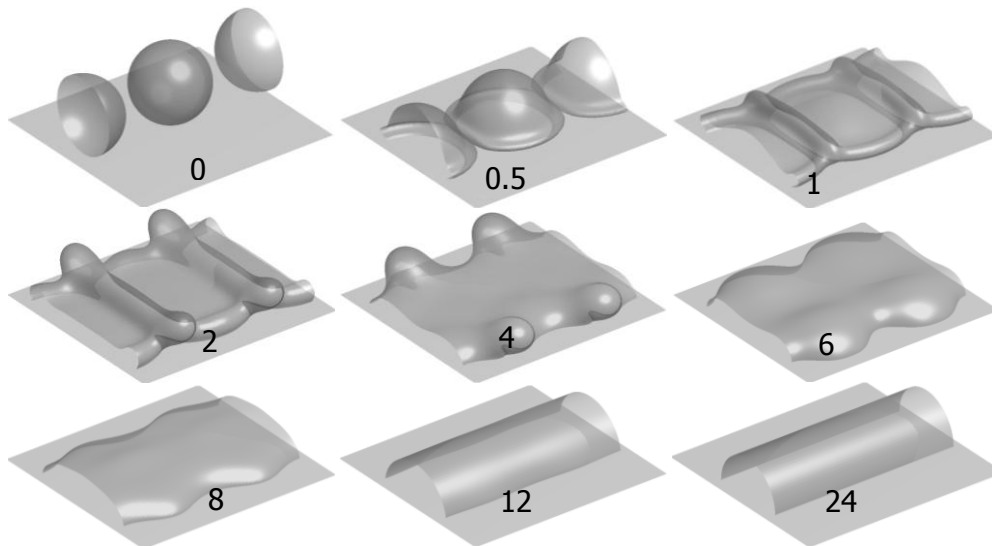

Figure 7. Demonstration of a-line-of-droplet impingement in the unit of dimensionless time (We = 100; Oh = 0.04; droplet distance = 65 μm).

These results demonstrated the LBM capability for handling highly complicated interface dynamics to become a powerful simulation tool to deepen our understanding of interfacial phenomena and a "digital design tool" for dynamic fluid interfaces of interest to many practical applications. The capability of handling complicated interfacial features can be utilized to optimize the manufacturing process for designs of complex geometrical features. The printing conditions and droplet distance (i.e., distance between nozzles) can also be optimized for targeted printing applications, such as printed electronics and thin-film patterning. As seen in Figure 7, lines can be formed readily under these material and interface conditions. The half-

cylindrical shape may be sufficient for a conductive line, but if it is meant to be one layer in a tall thin wall, the shape may cause difficulties when depositing subsequent layers. Referring to Figure 8, an interesting phenomenon is observed, where the droplet impact locations actually become voids in the thin film that forms from multiple droplets. Different material properties and different impingement conditions will yield films of different shapes, so the capability of simulating multiple conditions should prove beneficial when designing inkjet printing processes.
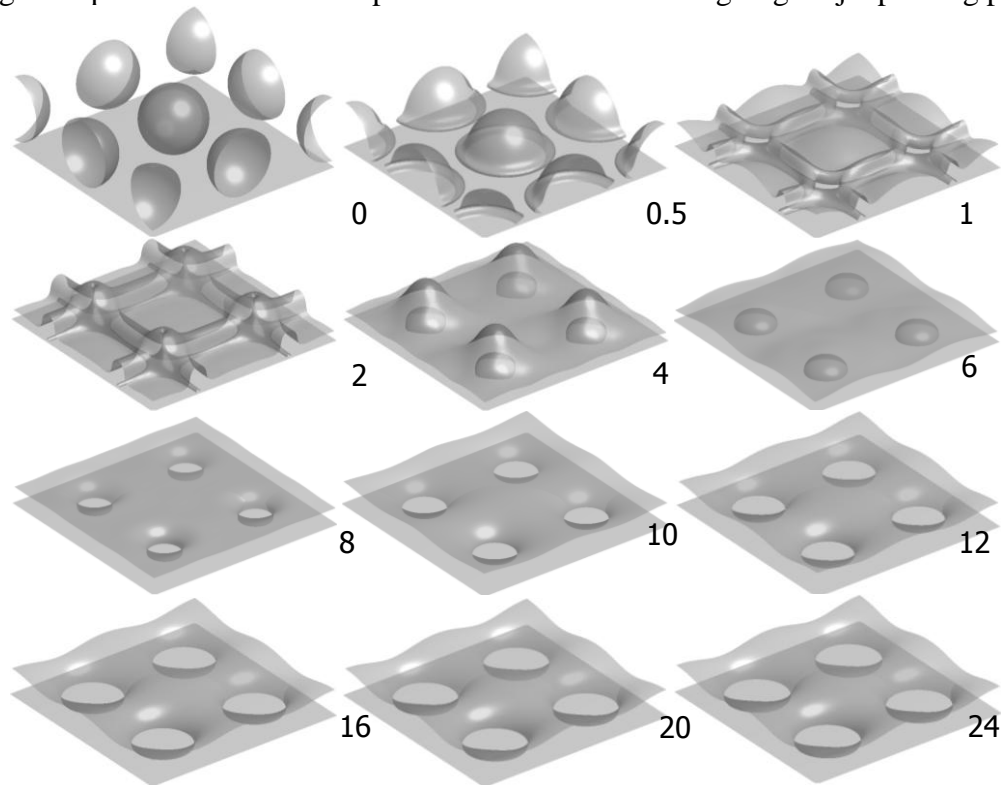

Figure 8. Demonstration of an-array-of-droplet impingement in the unit of dimensionless time (We = 100; Oh = 0.04; droplet distance = $80\,\mu m$).

6 CONCLUSIONS

A novel approach of solving the Navier-Stokes-based phase-field equations under isothermal conditions was proposed based on lattice Boltzmann method. The LBM evolution equations were derived for the distribution functions that were equivalent to the phase-field continuous governing equations through the Chapman-Enskog multiscale analysis. A new set of boundary conditions was also derived based on momentum conservation constraints and consistency with macroscopic boundary conditions to ensure correct hydrodynamics at the boundary. The simulation results were validated against COMSOL simulations, the LBM simulations reported in the literature, and experimental data. It was found that the proposed LBM formulation not only had significant improvement on computational efficiency but also produced better accuracy of predictions than COMSOL and the previous reported LBM models. The capability of the proposed LBM solver in handling highly complicated interface dynamics in 3D provides an approach of conducting "virtual experiments" for various interface phenomena involved in the inkjet deposition process, such as interface coalescence and interface breakup. Its computational efficiency in simulating multiple-droplet impingement provides a foundation for its utility in optimizing design of inkjet printers and printing processes for a variety of printing applications.

7 ACKNOWLEDGEMENT

8 REFERENCES

1.   A.M. Worthington, *On the forms assumed by drops of liquids falling vertically on a horizontal plate.* Proc. R. Soc. London, 1876. **25**: p. 261-271.

2.   E.B. Dussan, *On the spreading of liquids on solid surfaces: static and dynamic contact lines.* Annual Review of Fluid Mechanics, 1979. **11**: p. 371-400.

3.   Z. Zhao, D. Poulikakos, and J. Fukai, *Heat transfer and fluid dynamics during the collision of a liquid droplet on a substrate-II. Experiments.* International Journal of Heat and Mass Transfer, 1996. **39**: p. 2791-2802.

4.   H.Y. Kim and J.H. Chun, *The recoiling of liquid droplets upon collision with solid surface.* Physics of Fluids, 2001. **13**: p. 643-659.

5.   R. Rioboo, M. Marengo, and C. Tropea, *Time evolution of liquid drop impact onto solid, dry surfaces.* Experiments in Fluids, 2002. **33**: p. 112-124.

6.   S.E. Bechtel, D.B. Bogy, and F.E. Talke, *Impact of a liquid drop against a flat surface.* IBM J. Res. Dev., 1981. **25**: p. 963.

7.   S. Chandra and C.T. Avedisian. *On the collision of a droplet with a solid surface*. in *Proceedings of the Royal Society, Series A*. 1991. London.

8.   G. McHale, S.M. Rowan, and M.I. Newton, *Frenkel's method and the spreading of small sperical droplets.* J. Phys. D, 1994. **27**: p. 2619.

9.   T. Mao, D.C.S. Kuhn, and H. Tran, *Spread and rebound of liquid droplets upon impact on flat surfaces.* AIChE J., 1997. **43**: p. 2169.

10.   N. Hatta, H. Fujimoto, and H. Takuda, *Deformation process of a water droplet impinging on a solid surface.* Journal of Heat Transfer, 1995. **117**: p. 394-401.

11.   M. Bussmann, J. Mostaghimi, and S. Chandra, *On a three-dimensional volume tracking model of droplet impact.* Physics of Fluids, 1999. **11**: p. 1406-1417.

12.   M. Bussmann, S. Chandra, and J. Mostaghimi, *Modeling the splash of a droplet impacting a solid surface.* Physics of Fluids, 2000. **12**: p. 3121-3132.

13.   W. Zhou, et al., *Droplet impingement dynamics in ink-jet deposition.* Virtual and Physical Prototyping, 2012. **7**(1): p. 49-64.

14.   W. Zhou, et al., *What controls dynamics of droplet shape evolution upon impingement on a solid surface?* AIChE Journal, 2013: p. n/a-n/a.

15.   G.R. McNamara and G. Zanetti, *Use of the Boltzmann Equation to Simulate Lattice-Gas Automata.* Physical Review Letters, 1988. **61**(20): p. 2332-2335.

16.   X. Shan and H. Chen, *Lattice Boltzmann model for simulating flows with multiple phases and components.* PHYSICAL REVIEW E, 1993. **47**(3): p. 1815-1819.

17.   X. Shan and H. Chen, *Simulation of nonideal gases and liquid-gas phase transitions by the lattice Boltzmann equation.* PHYSICAL REVIEW E, 1994. **49**(4): p. 2941-2948.

18.   M.R. Swift, et al., *Lattice Boltzmann simulations of liquid-gas and binary fluid systems.* PHYSICAL REVIEW E, 1996. **54**(5): p. 5041-5052.

19.   M.R. Swift, W.R. Osborn, and J.M. Yeomans, *Lattice Boltzmann Simulation of Nonideal Fluids.* Physical Review Letters, 1995. **75**(5): p. 830-833.

20. X. He, S. Chen, and R. Zhang, *A Lattice Boltzmann Scheme for Incompressible Multiphase Flow and Its Application in Simulation of Rayleigh–Taylor Instability.* Journal of Computational Physics, 1999. **152**(2): p. 642-663.

21. X. He, X. Shan, and G.D. Doolen, *Discrete Boltzmann equation model for nonideal gases.* PHYSICAL REVIEW E, 1998. **57**(1): p. R13-R16.

22. T. Inamuro, et al., *A lattice Boltzmann method for incompressible two-phase flows with large density differences.* Journal of Computational Physics, 2004. **198**(2): p. 628-644.

23. T. Lee and C.-L. Lin, *A stable discretization of the lattice Boltzmann equation for simulation of incompressible two-phase flows at high density ratio.* Journal of Computational Physics, 2005. **206**(1): p. 16-47.

24. Y.Y. Yan and Y.Q. Zu, *A lattice Boltzmann method for incompressible two-phase flows on partial wetting surface with large density ratio.* Journal of Computational Physics, 2007. **227**(1): p. 763-775.

25. A.J. Briant, A.J. Wagner, and J.M. Yeomans, *Lattice Boltzmann simulations of contact line motion. I. Liquid-gas systems.* PHYSICAL REVIEW E, 2004. **69**(3): p. 031602.

26. A.J. Briant and J.M. Yeomans, *Lattice Boltzmann simulations of contact line motion. II. Binary fluids.* PHYSICAL REVIEW E, 2004. **69**(3): p. 031603.

27. T. Lee and L. Liu, *Lattice Boltzmann simulations of micron-scale drop impact on dry surfaces.* Journal of Computational Physics, 2010. **229**(20): p. 8045-8063.

28. H. Ding and P.D.M. Spelt, *Wetting condition in diffuse interface simulations of contact line motion.* PHYSICAL REVIEW E, 2007. **75**(4): p. 046708.

29. H. Kusumaatmaja and J. Yeomans, *Lattice Boltzmann Simulations of Wetting and Drop Dynamics*, in *Simulating Complex Systems by Cellular Automata*, J. Kroc, P.M.A. Sloot, and A.G. Hoekstra, Editors. 2010, Springer Berlin Heidelberg. p. 241-274.

30. J. Latt, et al., *Straight velocity boundaries in the lattice Boltzmann method.* Physical Review E, 2008. **77**(5): p. 056703.

31. C. Zhou, P. Yue, and J.J. Feng, *Deformation of a compound drop through a contraction in a pressure-driven pipe flow.* International journal of multiphase flow, 2008. **34**(1): p. 102-109.

32. S. Chapman and T.G. Cowling, *The mathematical theory of non-uniform gases: an account of the kinetic theory of viscosity, thermal conduction and diffusion in gases*. 1991: Cambridge university press.

33. H. Dong, et al., *Temporally-resolved inkjet drop impaction on surfaces.* AIChE Journal, 2007. **53**(10): p. 2606-2617.

34. J. Latt, *Hydrodynamic limit of lattice Boltzmann equations*. 2007, University of Geneva.

35. Y.-H. Qian and S.-Y. Chen, *Dissipative and dispersive behaviors of lattice-based models for hydrodynamics.* PHYSICAL REVIEW E, 2000. **61**(3): p. 2712-2716.

36. S.V. Patankar, *Numerical heat transfer and fluid flow*. 1980: Taylor & Francis Group.

37. P. Yue, et al., *Phase-field simulations of interfacial dyanmics in viscoelastic fluids using finite elements with adaptive meshing.* J. Comp. Phys., 2006. **219**: p. 47-67.

38. D. Jacqmin, *Calculation of Two-Phase Navier–Stokes Flows Using Phase-Field Modeling.* Journal of Computational Physics, 1999. **155**(1): p. 96-127.

39. T. Lee, C.-L. Lin, and L.-D. Chen, *A lattice Boltzmann algorithm for calculation of the laminar jet diffusion flame.* Journal of Computational Physics, 2006. **215**(1): p. 133-152.

40. W. Zhou, et al. *Impact of polyurethane droplets on a rigid surface for ink-jet printing manufacturing*. in *Solid Freeform Fabrication Symposium 2010*. 2010. Austin, TX.

41. W. Zhou, et al. *Shape Characterization for Droplet Impingement Dynamics in Ink-jet Deposition*. in *ASME 2012 International Design Engineering Technical Conference & Computers and Information in Engineering Conference*. 2012 Chicago, Illinois, USA.